High temperature H_2S removal via CO_2-assisted chemical looping over ZrO_2-modified Fe_2O_3

Jiawei Hu [a,b], Hilde Poelman [a], Stavros-Alexandros Theofanidis [a,c], Jonas J. Joos [d], Christophe Detavernier [e], Dirk Poelman [d], Wei Wei [b], Vladimir V. Galvita [a,*]

[a] Laboratory for Chemical Technology, Ghent University, Technologiepark 125, 9052 Ghent, Belgium
[b] Center for Low-Carbon Conversion Science and Engineering, Shanghai Advanced Research Institute, Chinese Academy of Sciences, No. 99 Haike Road, Zhangjiang Hi-Tech Park, Shanghai 201210, China
[c] AristEng S.à r.l., 77, Rue de Merl, L-2146, Luxembourg City, Luxembourg
[d] LumiLab research group, Ghent University, Krijgslaan 281, S1, 9000 Ghent, Belgium
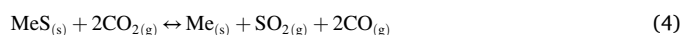[e] CoCooN research group, Ghent University, Krijgslaan 281, S1, 9000 Ghent, Belgium

ABSTRACT

Removal of H_2S via hot gas desulfurization demands more advanced and efficient processes to meet the environmental and economic requirements of modern industry. Hereto, we propose a novel process, termed CO_2-assisted Chemical Looping Hot Gas Desulfurization (CCLHGD), that involves alternating H_2S-induced sulfurization and CO_2-enabled regeneration of a core-shell structured ZrO_2-modified Fe_2O_3 oxygen carrier. Such CCLHGD process can be isothermally implemented at 750 °C with Ar-diluted model reactants, i.e., 50 % H_2 and 50 ppm H_2S for sulfurization and 10 % CO_2 for regeneration, wherein all H_2S is captured and next released as SO_2. Fe_2O_3 undergoes a stepwise sulfurization (with Fe_3O_4 and Fe as intermediates) towards iron sulfides, while the latter can be completely regenerated to iron oxides by CO_2. The thermally stable ZrO_2 in the core-shell structure contributes to resist sintering of the sulfurized iron particles, leading to good regenerability by oxidation with CO_2. This work demonstrates an efficient chemical looping scheme for H_2S removal, providing new opportunities for hot gas desulfurization.

1. Introduction

Hydrogen sulfide (H_2S) is one of the most significant and troublesome impurities in the feedstocks and/or products of many industrial processes, such as natural gas and biogas reforming, coal and biomass gasification, or petroleum refining [1,2]. Apart from its toxicity [3,4], H_2S is strongly corrosive to transport pipelines and production facilities and extremely poisonous toward catalysts, even at very low ppm levels [2,5,6]. Removal of H_2S from gas streams, prior to their utilization, is therefore of paramount importance for environmental protection and safe operation. The latter can be done at low temperature (< 300 °C), e.g., for cleanup of natural gas or biogas, while syngas produced in a gasifier requires high-temperature removal (700 °C and more). Owing to its high-temperature applicability, hot gas desulfurization (HGD), which improves the overall thermal efficiency and reduces the capital cost by eliminating the heat exchange, is receiving increased attention in energy and chemical industries, such as in the integrated gasification combined cycle (IGCC) power plants for the purification of coal- or biomass-derived syngas [7–9].

In a conventional HGD process, metal oxide (MeO) sorbents (such as ZnO, MnO_2, CuO, MgO, CaO, CeO_2, TiO_2 and Fe_2O_3 [7, 10–14]) are converted to metal sulfides (MeS) by capturing H_2S from the target stream under reducing hot gas conditions (Eq. 1). After the adsorption has saturated, the spent sorbents are regenerated (partially or completely) by using O_2 (Eqs. 2–3).

$$MeO_{(s)} + H_2S_{(g)} \leftrightarrow MeS_{(s)} + H_2O_{(g)} \tag{1}$$

$$MeS_{(s)} + 3/2O_{2(g)} \leftrightarrow MeO_{(s)} + SO_{2(g)} \tag{2}$$

$$MeS_{(s)} + 2O_{2(g)} \leftrightarrow MeSO_{4(s)} \tag{3}$$

$$MeS_{(s)} + 2CO_{2(g)} \leftrightarrow Me_{(s)} + SO_{2(g)} + 2CO_{(g)} \tag{4}$$

* Corresponding author.
  E-mail address: Vladimir.Galvita@UGent.be (V.V. Galvita).

$$Me_{(s)} + CO_{2(g)} \leftrightarrow MeO_{(s)} + CO_{(g)} \qquad (5)$$

This HGD process follows a scheme as in chemical looping oxidation (CLO), describing a specific type of redox scheme. In CLO, a given reaction is divided into two, temporally or spatially separated sub-steps bridged by an oxygen carrier material (OCM, commonly a metal oxide), which is periodically reduced (i.e., lattice oxygen consumption, by feedstocks to be converted) and re-oxidized (i.e., lattice oxygen replenishment, by oxygen donors) with appropriate reaction conditions for each step [15–19]. From chemical looping point of view, a conventional HGD implemented over an OCM serving as H_2S sorbent is also a cyclic two-step process, involving the reduction of the OCM by H_2S (i.e., sulfurization step) followed by the re-oxidation of the reduced OCM by O_2 (i.e., regeneration step), where H_2S is captured in the first step (Eq. 1) and released as SO_2 in the second step (Eq. 2). However, the oxidation of MeS into MeO by O_2 is highly exothermic (Fig. S1, Supplementary Information), which easily results in local overheating of the sorbents, thereby leading to particle sintering [20]. Although this problem can be mitigated by lowering the operating temperature of the regeneration step, the repetition of reactor cooling and heating cycles will certainly increase the energy penalty of the entire process. Furthermore, excess O_2 (i.e., higher partial pressure of O_2 relative to SO_2) is prone to react with MeS to form metal sulfates (MeSO$_4$) (Eq. 3) (Fig. S1). Since there is a large molar volume difference between MeO or MeS and MeSO$_4$, a structural expansion of the solid sorbent will occur, which leads to blockage of pores and an increase of the mass transfer resistance, consequently resulting in a loss of capture capacity [10,21, 22].

In this work, we propose a new process for high temperature H_2S removal, termed CO_2-assisted Chemical Looping Hot Gas Desulfurization (CCLHGD), which involves isothermally alternating H_2S-induced sulfurization and CO_2-enabled regeneration of an OCM. Compared to conventional HGD, CCLHGD provides many benefits: (i) CO_2 is a milder oxidant than O_2, thus, the strong exothermicity of the regeneration step is eliminated (Fig. S1). Additionally, the formation of metal sulfates can be exempted, as the oxidation of MeS into MeSO$_4$ by CO_2 is thermodynamically unfavorable; (ii) the isothermal process allows for its implementation in a single reactor column via straightforward switching of the gas feed, thereby decreasing operating costs and energy consumption; (iii) it shows great potential in integrating material regeneration and CO_2 conversion (Eqs. 4–5) [23]; (iv) through rationally tailoring the CO_2 affinity of the OCM, the regeneration rate of the sulfurized material as well as the CO_2 conversion performance can be enhanced, since the regeneration is now achieved by the oxidation of MeS into MeO by lattice O originating from CO_2 dissociation.

The key to success of CCLHGD is the employment of a suitable OCM, which should afford high H_2S capture capacity, reasonable adsorption kinetics, high-temperature stability and good regenerability by CO_2 [10]. From these aspects, a Fe_2O_3-based material emerges as the best candidate, due to its high H_2S uptake (even in reducing atmosphere), low price, facile regeneration and high capability for oxygen storage from CO_2 [1,7,15,20,24–29]. However, as iron oxide particles easily sinter during high-temperature reactions, the introduction of a stabilizer is necessary to enhance the sintering resistance of the material. ZrO_2 is widely considered as a good option, not only because of its thermal stability, but also for its contribution to oxygen ion mobility [29,30]. Although in a Fe_2O_3-ZrO_2 material Fe_2O_3 is the main sorbent for H_2S, interaction between ZrO_2 and H_2S may facilitate both sulfurization and regeneration processes: dissociative adsorption of H_2S on the ZrO_2 surface enhances the H_2S decomposition [31,32], while the substitution of sulfur into the ZrO_2 lattice can improve the mobility of its surface lattice oxygen, thereby enhancing the material's redox ability [33,34]. In our previous work [35], a core-shell structured $Fe_2O_3/ZrO_2@ZrO_2$ OCM was synthesized with a nano-Fe_2O_3/ZrO_2 core and a mesoporous ZrO_2 shell, which showed enhanced activity and stability for cyclic CO_2 conversion at high temperature. Therefore, by employing the $Fe_2O_3/ZrO_2@ZrO_2$

OCM as H_2S sorbent, this work focuses on verifying the feasibility of the isothermal CCLHGD process, while investigating the possible reaction mechanisms of the proposed process.

2. Experimental

2.1. Materials preparation

The $Fe_2O_3/ZrO_2@ZrO_2$ material was synthesized by a nanocoating method, during which a porous ZrO_2 nanoshell was deposited on a Fe_2O_3/ZrO_2 core material. The latter was prepared by incipient wetness impregnation upon the ZrO_2 support using an aqueous solution containing the required amount of $Fe(NO_3)_3 \cdot 9H_2O$ (99.99 + %, Sigma-Aldrich). The impregnated powder was kept overnight at room temperature, then dried at 120 °C for 4 h and calcined at 400 °C (heating rate: 1 °C min^{-1}) for 1 h. Afterwards, an ethanol suspension containing the required amount (based on the predetermined Fe_2O_3 loading in the final product: 15 wt. %) of the core material was heated to 30 °C under vigorous stirring, then a P-123 (average $M_n \sim 5800$, Sigma-Aldrich) aqueous solution (4 wt. % in water) was added. After 1 h, an appropriate amount of zirconium propoxide solution (70 wt. % in 1-propanol, Sigma-Aldrich) was added dropwise and kept under stirring for 20 h at 30 °C. The collected product was calcined at 700 °C (heating rate: 1 °C min^{-1}) for 4 h, to form the porous ZrO_2 shell. More details regarding the preparation of this core-shell material can be found elsewhere [35].

Bare Fe_2O_3 material was obtained by direct calcination of Fe_2O_3 nanopowder (γ-phase, 100 %, Sigma-Aldrich) at 700 °C (heating rate: 1 °C min^{-1}) for 4 h. The ZrO_2 support was prepared by precipitation through addition of excess ammonium hydroxide (28.0 − 30.0 % NH_3 basis, Sigma-Aldrich) to an aqueous solution of $ZrO(NO_3)_2 \cdot 6 H_2O$ (99 %, Sigma-Aldrich). The collected precipitate was washed with de-ionized water, dried at 120 °C for 4 h and calcined at 900 °C (heating rate: 5 °C min^{-1}) for 2 h.

2.2. Material characterization

Inductively coupled plasma-atomic emission spectrometry (ICP-AES, instrument ICAP 6500 from Thermo Scientific) was applied to determine the actual Fe_2O_3 loading, which was 15 wt. %. The textural properties of the fresh materials were measured by N_2 adsorption-desorption at −196 °C in a Gemini Micromeritics apparatus. The specific surface area was determined by the five-point method of the Brunauer-Emmett-Teller theory. Pore volume and average pore size were determined by the classical Barrett-Joyner-Halenda method. The changes in morphological structure and elemental distribution of the materials after sulfurization and regeneration were examined by high-angle annular dark field scanning transmission electron microscopy (HAADF-STEM), combined with energy dispersive X-ray (EDX) spectroscopy, using a JEOL JEM-2200FS Cs-corrected microscope equipped with a Schottky-type field emission gun (operated at 200 kV) and a JEOL JED-2300D energy dispersive X-ray detector. Specimens were prepared by evenly dispersing the sample powder onto a copper grid with a lacey carbon film. Randomly-chosen particles were used to take STEM images and EDX elemental mappings. The chemical state of sulfur on the surface of sulfurized material was analyzed by X-ray photoelectron spectroscopy (XPS) in a S-Probe XPS spectrometer (VG, Surface Science Instruments) equipped with a monochromatized Al Kα source. The base pressure of the analysis chamber was below 2×10^{-7} Pa. Spectra were recorded with 200 W source power. Wide scan and narrow windows were measured with pass energies of 157 eV (0.22 eV step) and 107.8 eV (0.10 eV step), respectively.

The crystal phases of the materials at different stages (fresh, sulfurized, regenerated) were determined by powder X-ray diffraction (XRD) measurement, using a Siemens Diffractometer Kristalloflex D5000 with Cu Kα radiation (0.154 nm wavelength). XRD patterns were collected in

a 2θ range of 25° – 55° with a step of 0.02° and 30 s counting time per angle. Known compounds with characteristic diffraction peaks are referred to by their corresponding number in the powder diffraction file database. Crystallite size (nm) and interplanar distance (nm) of a phase were estimated based on Scherrer's equation [36] and Bragg's law [37], respectively, after Gaussian fitting.

The crystallographic changes of $Fe_2O_3/ZrO_2@ZrO_2$ during H_2-CO_2 redox cycles were followed by time-resolved in-situ XRD using a Bruker-AXS D8 Discover apparatus with a linear detector, equipped with an in-house built reactor with X-ray transparent Kapton windows (Cu Kα radiation, covered 2θ range: 20°, angular resolution: 0.1°, pattern collection time: 10 s). A rig with calibrated mass flow controllers was connected to the chamber for gas feeding. The sample temperature was measured using a K-type thermocouple and corrected using a dedicated calibration curve for the heating stage. 20 mg of powder material was spread over a Si sample holder, which did not react with the sample in the applied temperature range. The reactor chamber was evacuated to 4 Pa and purged with He for 10 min before admitting reactive gases. H_2-CO_2 redox cycles were carried out at 750 °C with alternating reduction (5 vol. % H_2 in He) and re-oxidation (pure CO_2) sequences, after quickly ramping up to the target temperature under He (at 60 °C min^{-1}). Each cycle consisted of 2 min material reduction, 2 min material re-oxidation and twice 4 min He purging in between (total of 12 min). All gas flow rates were 60 mL min^{-1}.

The evolution of sulfur species over $Fe_2O_3/ZrO_2@ZrO_2$ during sulfurization and regeneration was investigated through X-ray absorption spectroscopy (XAS) at the LUCIA beamline of the SOLEIL synchrotron in France. XAS was measured in fluorescence mode at the S K-edge (2472 eV) under vacuum conditions (to limit atmospheric absorption). 2D XAS color contours were recorded in-situ during sulfurization of pelletized fresh material by a mixture of H_2 and H_2S (250 ppm H_2S + 2.5 vol. % H_2 in He) at 500 °C, as well as during isothermal regeneration of this sulfurized material by CO_2 (30 vol. % CO_2 in He). The flow rate of the feed gases was 50 mL min^{-1}. The sulfurization or regeneration level of the material was assessed by the exposure time to the reactant gas, i. e., the H_2 - H_2S mixture or CO_2, varying from 0 min to 120 min. In each stage (fresh, sulfurized and regenerated), X-ray absorption near-edge structure (XANES) spectra were measured in-situ to identify the sulfur species formed. Moreover, ex-situ measurements of XANES spectra at the S K-edge were recorded for materials pre-sulfurized under harsh conditions (750 °C, pure H_2S, for 1 min, 5 min or 30 min exposure) and regenerated at 700 °C with pure CO_2 for 30 min. Finally, 4 standard materials, such as S, Ni_3S_2, Cu_2S and $NH_4Fe(SO_4)_2$, were equally measured ex-situ to serve as references for S^0, S_2^{2-}, S^{2-} and SO_4^{2-}, respectively.

2.3. Reactor setup and procedures

The reaction assessments over the $Fe_2O_3/ZrO_2@ZrO_2$ material were performed at 750 °C and 1 bar in a quartz tubular microreactor (inner diameter: 6 mm), housed inside a tubular ceramic oven with approximately 10 cm length heating zone. The sample bed was composed of the material (50 mg) and diluent α-Al_2O_3 (1 g, for improving heat conductivity), well mixed and packed between quartz wool plugs, where the temperature was measured with K-type thermocouples, directly inside the sample bed and touching the outside of reactor at a fixed position nearby the sample bed. The inlet gas flow rates were maintained by Bronkhorst mass flow controllers, calibrated with the corresponding gases. Prior to reaction, the reactor was purged with Ar for 10 min, after which the sample bed was heated to 750 °C (ramping rate: 10 °C min^{-1}) under Ar flow (for experiments starting from fresh material). For experiments starting from reduced material, the purge was followed by a 1 min exposure to 10 vol. % H_2 in Ar at 750 °C. After purging, sulfurization experiments were performed by feeding a H_2S and H_2 mixture diluted with Ar (H_2S concentration varying from 0 to 100 ppm) for 6 min. One cycle of the isothermal CCLHGD process was implemented

on the fresh $Fe_2O_3/ZrO_2@ZrO_2$ material, composed of 2 min sulfurization by an Ar-diluted H_2 (50 %) and H_2S (50 ppm) mixture, 10 min regeneration by 10 vol. % CO_2/Ar, and 4 min Ar purging in between. All gas flow rates were 100 mL min^{-1}. The outlet sulfur-bearing products were detected after a cold trap using a gas chromatograph (GC, Thermo TRACE1300) equipped with a flame photometric detector (FPD). The duration of each GC analysis was 2 min

2.4. Thermodynamic calculations

The EkviCalc software (Ekvicalc and Ekvibase, version 4.30; Svensk Energi Data: Balinge, Sweden, 2013) was employed to calculate the Gibbs free energy of the related reactions. Given the initial amount of reactant and the chemical species that are considered as possible products, thermodynamic parameters at a specified temperature and pressure can be calculated according to the criterion of Gibbs free energy minimization (Eq. 6), yielding equilibrium data (molar amount, partial pressure, enthalpy, entropy, heat capacity and free energy) of all involved species as well as thermodynamic properties of the corresponding reaction (enthalpy, entropy, free energy and their changes):

$$dG_{p,T} = \sum_{i=1}^{m} \mu_i dn_i = 0 \tag{6}$$

where m (-) is the number of reactant and product species, μ_i (J mol^{-1}) is the chemical potential of species i at pressure p (bar) and temperature T (K), n_i (mol) is the amount of species i, and $G_{p,T}$ (J) is the Gibbs free energy of the system at pressure p and temperature T.

3. Results and discussion

3.1. Isothermal hot gas desulfurization over ZrO_2-modified Fe_2O_3

Compared to bare Fe_2O_3, $Fe_2O_3/ZrO_2@ZrO_2$ has higher specific surface area and pore volume (Table S1), all important properties for an efficient H_2S sorbent. Moreover, $Fe_2O_3/ZrO_2@ZrO_2$ possesses a comparable sulfur capacity based on H_2S breakthrough as e.g. a conventional Fe_2O_3/Al_2O_3 sorbent with the same Fe_2O_3 loading (Fig. S2 and Table S2). Hence, the feasibility of the isothermal CCLHGD process was investigated at lab-scale over the $Fe_2O_3/ZrO_2@ZrO_2$ OCM, employing sulfurization with a model mixture of H_2 and H_2S, followed by regeneration with CO_2. The sulfur-bearing products during the sulfurization and regeneration of $Fe_2O_3/ZrO_2@ZrO_2$ at 750 °C are displayed in Fig. 1. Overall, no H_2S is detected in any of the present experiments, indicating that $Fe_2O_3/ZrO_2@ZrO_2$ has the capacity for complete H_2S removal from a hot gas stream under the applied conditions. During sulfurization with a H_2S (100 ppm) only feed (Fig. 1a), the formation of SO_2 over the fresh material indicates that H_2S is oxidized by lattice oxygen of Fe_2O_3, while the latter is reduced (e.g., following Reaction 1 in Fig. S3). Over fully reduced material, confirmed by in-situ XRD characterization (Fig. S4), neither H_2S nor SO_2 are detected (Fig. 1b), indicating that direct sulfurization of Fe takes place (Reaction 3 in Fig. S3). When sulfurizing the fresh material with a mixture of H_2 (10 %) and H_2S (90 ppm) (Fig. 1c), SO_2 formation shows a lower and constant yield than with the H_2S only feed (Fig. 1a), implying competition between H_2 and H_2S for the lattice oxygen of Fe_2O_3, because the reduction of Fe_2O_3 by H_2 occurs in parallel. The latter however not necessarily compromises the uptake of H_2S as iron in reduced state (such as Fe_3O_4, metallic Fe and FeS) easily reacts with H_2S to form iron sulfides (Reactions 2–4 in Fig. S3). In a full CCLHGD cycle (Fig. 1d), SO_2 is not detected during the 2 min sulfurization step with a feed of 50 % H_2 and 50 ppm H_2S, similar to the result observed over the reduced material (Fig. 1b). This is ascribed to the fact that under high H_2 concentrations (e.g., in coal- or biomass-derived syngas) Fe_2O_3 is rapidly reduced (by H_2) to low-valence iron, which is subsequently sulfurized (by H_2S) to iron sulfides without forming SO_2 (Reactions 2–3 in Fig. S3). Note that the formation of elemental sulfur is
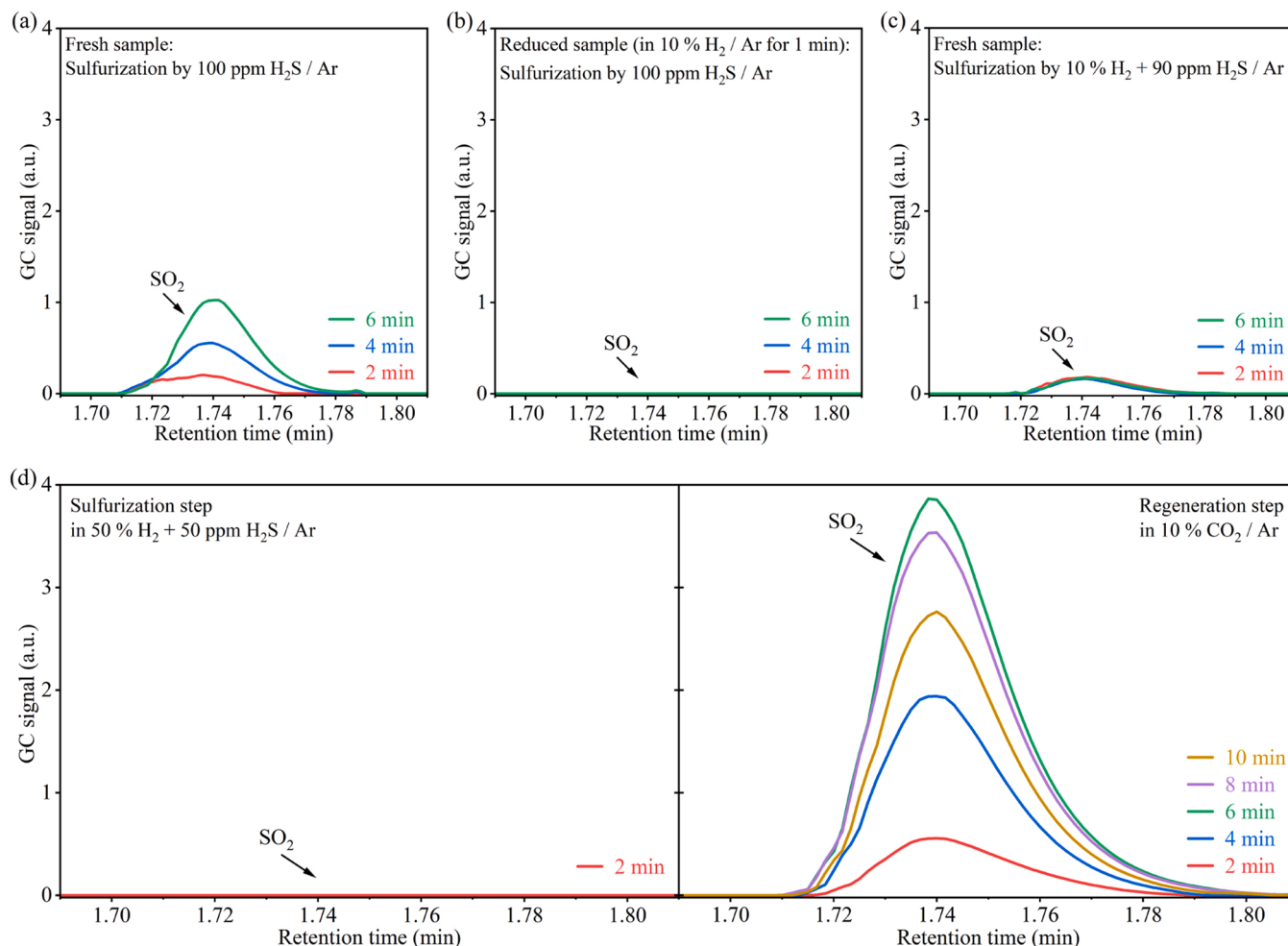
Fig. 1. Evolution of sulfur-bearing products during different processes: (a-c) sulfurization of the (a, c) fresh and (b) reduced (by 10 vol. % H_2 in Ar for 1 min) Fe_2O_3/ $ZrO_2@ZrO_2$ material by (a, b) 100 ppm H_2S in Ar or (c) 10 vol. % H_2 + 90 ppm H_2S in Ar; (d) isothermal CCLHGD process, composed of 2 min sulfurization (by 50 vol. % H_2 + 50 ppm H_2S in Ar), 10 min regeneration (by 10 vol. % CO_2 in Ar) and 4 min Ar purging in between, implemented on the fresh Fe_2O_3/ZrO_2 @ZrO_2 material. Experimental conditions: gas flow rates = 100 mL min^{-1}, sample mass = 50 mg, temperature = 750 °C.

also possible during the sulfurization process, since the Claus reaction (Reaction 5 in Fig. S3) and FeS_2 pyrolysis (Reactions 6–7 in Fig. S3) are thermodynamically favorable at 750 °C, which has also been confirmed in previous studies [38,39]. For the former, the produced SO_2 could further react with H_2S on the material surface, yielding H_2O and elemental sulfur; For the latter, the formed FeS_2 can decompose into FeS (or Fe_7S_8) and elemental sulfur. However, at a temperature above 100 °C, elemental sulfur is prone to sublimate into gaseous sulfur, which subsequently condenses in the cold trap behind the reactor, making it undetectable by gas chromatography.

During the regeneration step (Fig. 1d), SO_2 immediately forms when feeding CO_2, meaning that the accumulated sulfur (in the lattice or surface deposited) can be gasified by CO_2, which at the same time ensures regeneration of the sulfurized Fe_2O_3/ZrO_2 @ZrO_2 material. Moreover, SO_2 is the only sulfur-bearing product, with no COS detected, consistent with other experimental studies on the oxidation of FeS and FeS_2 by CO_2 at high temperature (400 °C − 1000 °C) [23,40,41]. This can be attributed to the significantly lower activation energy for SO_2 formation and the lower energy required for SO_2 desorption (99.0 kJ mol^{-1} and 202.3 kJ mol^{-1}, respectively), on a FeS_2 surface) compared to the values for COS formation and desorption (218.3 kJ mol^{-1} and 480.9 kJ mol^{-1}, respectively) [42].

In-situ XAS studies at the S K-edge visualize the H_2S-induced sulfurization and CO_2-enabled regeneration of Fe_2O_3/ZrO_2 @ZrO_2. Fig. 2a-b exhibit the elemental mappings of the material recorded after different

treatment durations. Significant changes in signal intensity are observed, showing an increase with time (i.e., sulfur capture) during sulfurization (Fig. 2a) and a decrease (i.e., sulfur removal) in the subsequent regeneration (Fig. 2b). Fig. 2c displays the XANES spectra of $Fe_2O_3/ZrO_2@ZrO_2$ at the S K-edge recorded after the above treatments. No representative peak for sulfur species is observed on the fresh sample. On the sulfurized sample, characteristic peaks related to elemental sulfur, sulfide and sulfate appear, confirming the sulfurization of Fe_2O_3/ $ZrO_2@ZrO_2$ by the mixture of H_2 (2.5 vol. %/He) and H_2S (250 ppm) at 500 °C. The XANES spectrum of the regenerated sample resembles that of the fresh one, meaning that most of the sulfur species are removed. This indicates that the sulfurized $Fe_2O_3/ZrO_2@ZrO_2$ is regenerated by CO_2 at the same temperature (500 °C), demonstrating that the proposed CCLHGD process can be implemented isothermally over the Fe_2O_3/ $ZrO_2@ZrO_2$ material.

3.2. Fe_2O_3 and ZrO_2 transformation under extreme conditions

To identify the role of Fe_2O_3 and ZrO_2 during sulfurization and regeneration, the $Fe_2O_3/ZrO_2@ZrO_2$ OCM was treated with H_2S and CO_2 under more harsh conditions to emphasize the respective changes. Fig. 3a displays the ex-situ XRD patterns of the $Fe_2O_3/ZrO_2@ZrO_2$ material, fresh and after exposure to pure H_2S at 750 °C for different timespans. ZrO_2 typically consists of coexisting monoclinic (m-) and tetragonal (t-) phases [42]. The main phase in the present
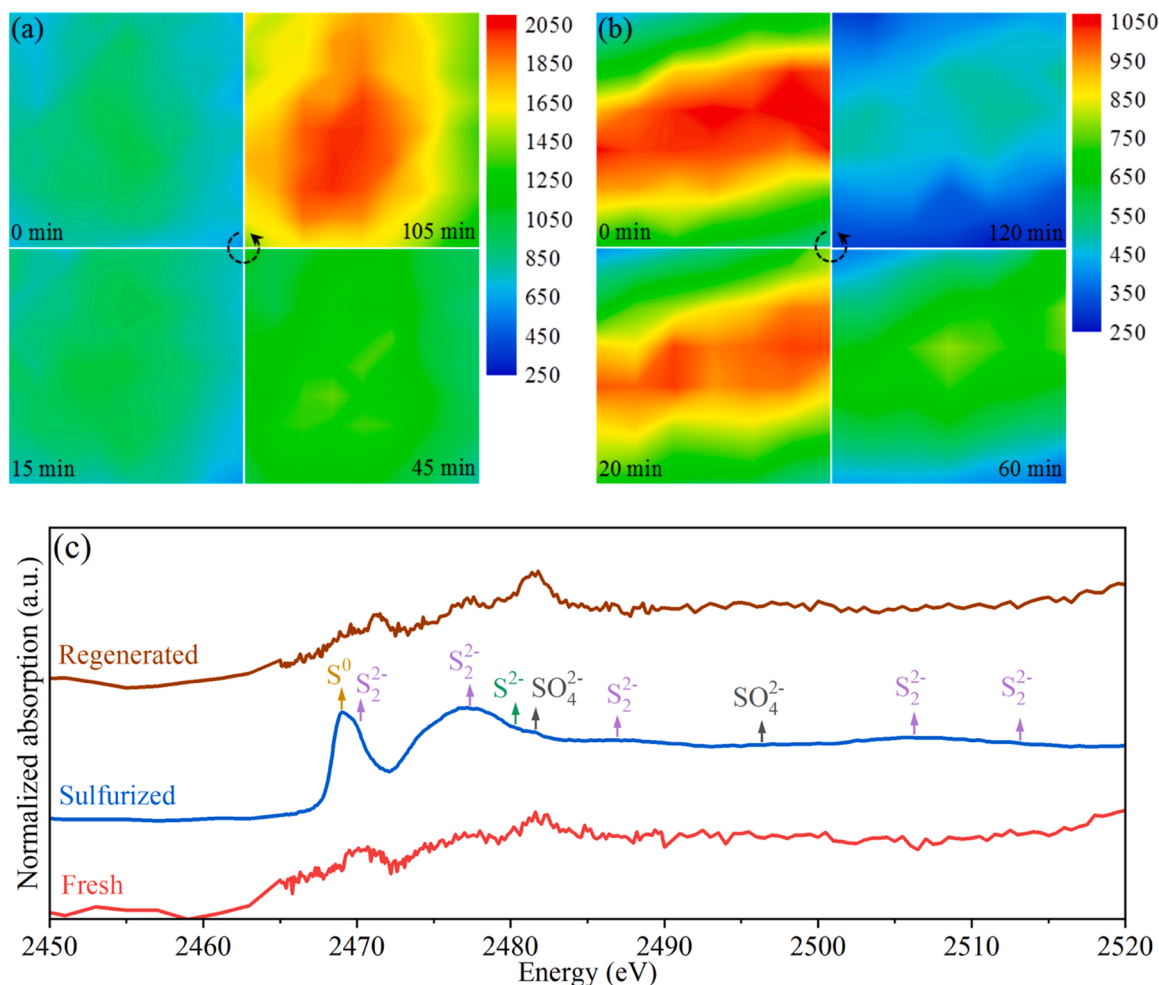
Fig. 2. 2D in-situ XAS spectra at the S K-edge, recorded during the (a) sulfurization of fresh and (b) regeneration of sulfurized Fe$_2$O$_3$/ZrO$_2$@ZrO$_2$ material at 500 °C. (c) in-situ XANES at the S K-edge for fresh, sulfurized and regenerated samples. Feed gases (50 mL min^{-1}): sulfurization: 250 ppm H$_2$S and 2.5 vol. % H$_2$ in He; regeneration: 30 vol. % CO$_2$ in He.
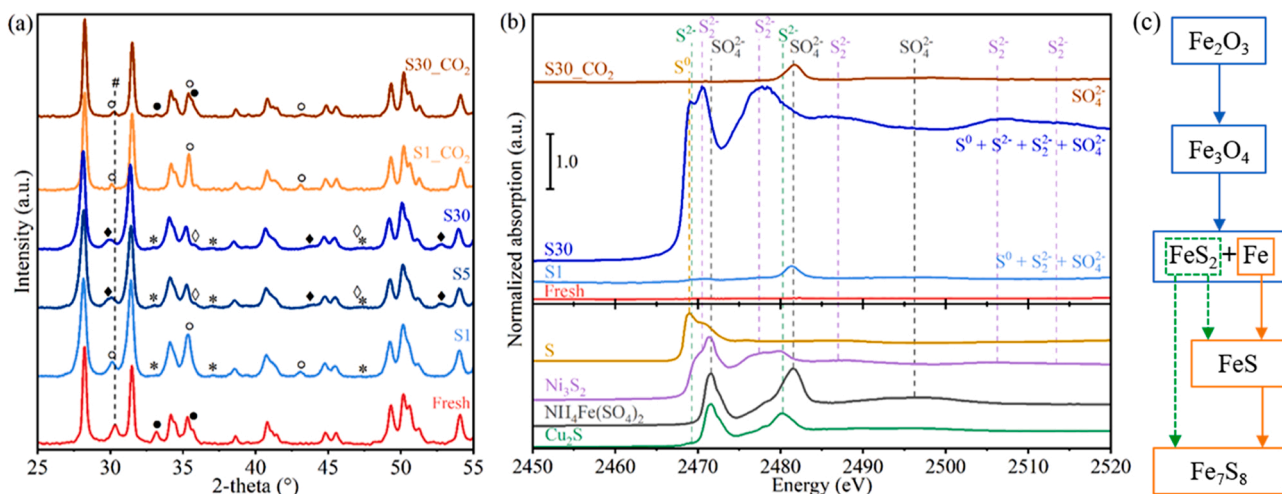

Fig. 3. (a) ex-situ XRD patterns of the Fe$_2$O$_3$/ZrO$_2$@ZrO$_2$ material in fresh, sulfurized and regenerated states. The sulfurization treatment was performed in pure H$_2$S at 750 °C for different durations, e.g., S1 represents 1 min sulfurization. The regeneration was performed using pure CO$_2$ at 700 °C for 30 min (the regenerated samples are marked with _CO$_2$). Symbols represent: ● – Fe$_2$O$_3$ (JCPDS: 33–0664); ○ – Fe$_3$O$_4$ (19–0629); ◇ – FeS (49–1632); ◆ – Fe$_7$S$_8$ (25–0411); *– FeS$_2$ (42–1340); # – t-ZrO$_2$ (80–2156). Unmarked diffraction peaks pertain to m-ZrO$_2$ (83–0944). (b) ex-situ XANES spectra at the S K-edge for the Fe$_2$O$_3$/ZrO$_2$ @ZrO$_2$ material in fresh, harshly sulfurized and regenerated state (top panel). The Cu$_2$S, NH$_4$Fe(SO$_4$)$_2$, Ni$_3$S$_2$ and S standards were measured ex-situ as references (bottom panel). Dashed lines indicate main identifier features of the standards. (c) a possible pathway proposed for the evolution of iron species in Fe$_2$O$_3$/ZrO$_2$@ZrO$_2$ during the high-temperature sulfurization process with pure H$_2$S, based on the experimental observations and thermodynamic calculations (Fig. S3).

$Fe_2O_3/ZrO_2@ZrO_2$ material is m-ZrO_2, with small contributions from t-ZrO_2 and Fe_2O_3. After 1 min sulfur exposure, Fe_2O_3 transforms into Fe_3O_4 and FeS_2 (Fig. 3a, pattern S1). Thermodynamics suggests that the reduction of Fe_2O_3 by H_2S, forming Fe_3O_4 and SO_2 (Reaction 1, Fig. S3), occurs spontaneously at 750 ºC. Furthermore, Fig. 1a shows that SO_2 is immediately produced when the fresh material comes in contact with H_2S at 750 ºC. Therefore, it can be deduced that Fe_2O_3 may initially be reduced to Fe_3O_4 during the sulfurization with H_2S, which is consistent with previous work [7]. In addition, Fe_3O_4 is considered a direct reactant for the formation of FeS_2 (Reaction 2, Fig. S3) [43]. Hence, Fe_3O_4 and FeS_2 are the main phases in the sulfurized material after a short H_2S treatment. Upon prolonged exposure (5 or 30 min), Fe_3O_4 disappears, while besides FeS_2, FeS and Fe_7S_8 form (Fig. 3a, patterns S5 and S30). These imply the further transformation of Fe_3O_4 to FeS_2 and Fe (Reaction 2, Fig. S3), thereafter the metallic Fe can be successively sulfurized to FeS, and then to Fe_7S_8 (Reactions 3–4, Fig. S3). To further confirm the evolution of iron species in $Fe_2O_3/ZrO_2@ZrO_2$ mentioned above, XPS characterization of the $Fe\ 2p_{3/2}$ photo line for the materials in different state was performed (Fig. S5). Fresh $Fe_2O_3/ZrO_2@ZrO_2$ shows a peak at 709.6 eV, consistent with the characteristics of reference Fe_2O_3 [44]. After sulfurization for 1 min (spectrum S1), two major peaks at 706.7 and 710.8 eV appear, which can be attributed to the formation of FeS_2 and Fe_3O_4, respectively [45,46]. After sulfurization for 5 min (spectrum S5), the peak at 706.7 eV for FeS_2 remains, while three new peaks at 708.5, 710.6 and 713.3 eV indicate the formation of FeS and Fe_7S_8, respectively [47,48].

Fig. 3b shows the ex-situ XANES patterns of $Fe_2O_3/ZrO_2@ZrO_2$ in different stages. On the material sulfurized at 750 °C (patterns S1 and S30), besides sulfides (S_2^{2-} and S^{2-}), also elemental sulfur (S^0) is observed, which accumulates with the extension of sulfurization time, thereby confirming the hypothesis of Section 3.1. As shown by XPS of the sulfurized materials (Fig. S5), the surface concentration of FeS_2 significantly decreases with the formation of FeS and Fe_7S_8, implying the occurrence of FeS_2 pyrolysis. Hence, during sulfurization of $Fe_2O_3/ZrO_2@ZrO_2$, the latter lies also at the origin of elemental sulfur in addition to the Claus reaction. Furthermore, a noteworthy signature of SO_4^{2-} appears on all the treated materials, indicating the formation of sulfate species. However, XRD does not identify a crystalline $FeSO_4$ phase in these materials (Fig. 3a), likely because at high temperature, $FeSO_4$ is very unstable: at 750 °C for instance, even though $FeSO_4$ forms (Reaction 8 in Fig. S3), it will decompose immediately, releasing gaseous SO_x (Reaction 9 in Fig. S3). Based on the above results, a possible evolution pathway of the iron species in $Fe_2O_3/ZrO_2@ZrO_2$ during high-temperature sulfurization is drawn in Fig. 3c, showing a stepwise transformation of Fe_2O_3 to iron sulfides (FeS_2, FeS and Fe_7S_8) with Fe_3O_4 and Fe as intermediates. The sulfate observed in XANES most likely forms on ZrO_2. To examine this, the ZrO_2 support was exposed to the same sulfurization process (i.e., pure H_2S at 750 °C) and characterized. STEM-EDX mapping clearly shows the presence of sulfur-related substances on ZrO_2 after sulfurization (Fig. S6a). The XPS S 2p photo line for the sulfurized ZrO_2 shows a significant peak located at ~168 eV (Fig. S7), corresponding to sulfur in sulfates [49–51], which further confirms the formation of SO_4^{2-} on the surface of ZrO_2 after sulfurization. The increasing intensity of the SO_4^{2-} peak over time (Fig. S7) indicates that sulfur accumulates on ZrO_2.

H_2S adsorbed on ZrO_2 at high temperature has a high tendency to exchange sulfur with lattice oxygen at low coordination sites ($H_2S + O^{2-} \rightarrow H_2O + S^{2-}$) [31–33, 52]. Such phenomenon can also occur on the $Fe_2O_3/ZrO_2@ZrO_2$ material during sulfurization. Compared to fresh material, the characteristic diffraction peaks of m-ZrO_2 (at $2\theta = 28.2°$ and 31.5°) in the sulfurized $Fe_2O_3/ZrO_2@ZrO_2$ shift to lower angle, corresponding to an increase of the interplanar distance (Fig. 4a). The latter can be attributed to the replacement of lattice O (atomic radius = 0.066 nm) by a larger atom (such as S, atomic radius = 0.104 nm), inducing expansion of the crystal lattice, which leads to a decreased diffraction angle, following Bragg's law [37]. Such replacement of O by
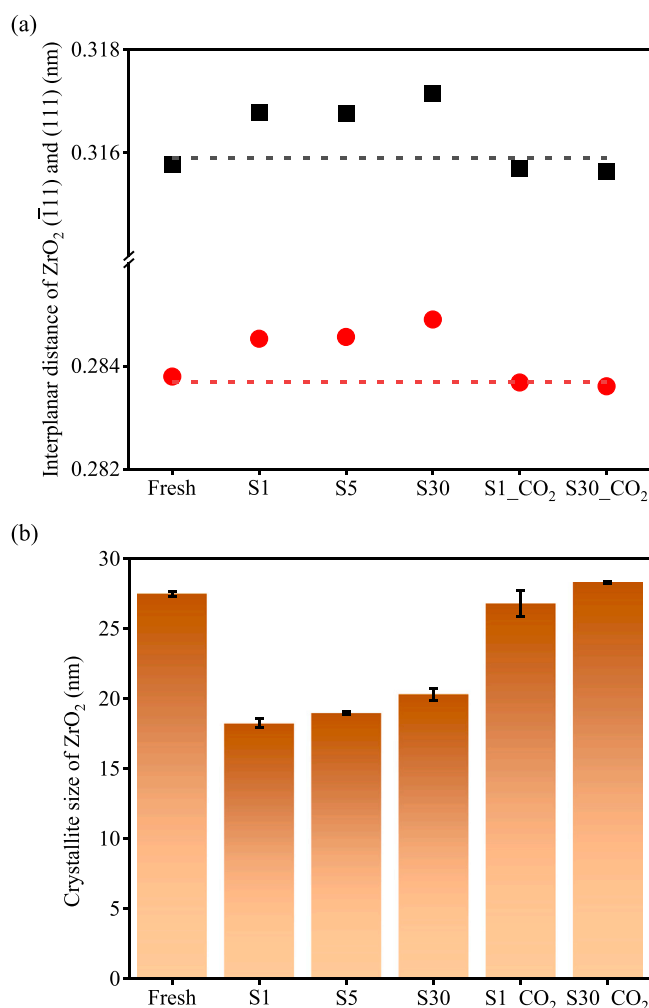

Fig. 4. (a) Interplanar distance and (b) crystallite size of the m-ZrO_2 phase of $Fe_2O_3/ZrO_2@ZrO_2$ in fresh, sulfurized (by pure H_2S at 750 ºC for different durations) and regenerated (by pure CO_2 at 700 ºC for 30 min) states. Sample labels: Sx represents sulfurization for x min; the regenerated samples are marked with _CO_2 extension. Interplanar distance and crystallite size are estimated from Gaussian fitting of the two most intense diffraction peaks (at $2\theta = 28.2°$ and 31.5°, corresponding to the ■ ($\bar{1}11$) and ● (111) planes, respectively, see Fig. 3a). Dashed lines (figure a) represent the typical interplanar distance of the selected planes (JCPDS: 83–0944). Error bars (figure b) represent the standard deviation of the crystallite size.

S in the ZrO_2 lattice has been found to increase its surface basicity and oxygen mobility [33,53,54], enhancing its affinity towards CO_2. In addition, the substitution of S also distorts the ZrO_2 crystal structure, leading to a decrease in its crystallite size (Fig. 4b). The decrease in crystallite size due to the distortion of the pristine crystal structure with the atom substitution has been demonstrated in previous study [55].

Upon regeneration, all iron sulfide phases disappear and iron oxide phases are regained after CO_2 treatment at 700 °C (S1_CO_2 and S30_CO_2) (Fig. 3a). This is achieved by oxidation of the iron sulfides by oxygen originating from CO_2 dissociation (Fig. 2b). A DFT study on the oxidation of FeS_2 by CO_2 has confirmed that the dissociation of CO_2 is the initial step, followed by the binding of the two generated O atoms with S to form SO_2 [42]. Interestingly, the crystallite size of m-ZrO_2 in the regenerated $Fe_2O_3/ZrO_2@ZrO_2$ returns to that of the fresh material (Fig. 4b), signifying the recovery of the pristine crystal structure of m-ZrO_2. The latter is attributed to the resubstitution of S by O, implying the occurrence of CO_2 dissociation as only source of O atoms during regeneration. Moreover, the reversible replacement of O by S (i.e.,

consumption of lattice oxygen by H_2S during sulfurization, followed by replenishment of lattice oxygen by CO_2 during regeneration) occurring in the ZrO_2 lattice, will enhance the capability of this material to remove H_2S.

XANES spectra confirm the regeneration of $Fe_2O_3/ZrO_2@ZrO_2$ (S30 versus S30_CO₂, Fig. 3b), where only sulfate species remain on the regenerated sample (S30_CO₂), in evidence of the strong binding between SO_4^{2-} and ZrO_2. STEM-EDX mapping does show that most of the sulfur-related substances on the sulfurized ZrO_2 support cannot be removed by regeneration (Fig. S6b). In fact, under high-temperature ($> 700\ °C$) atmospheres, t-ZrO_2 easily transforms into m-ZrO_2 [56]. However, it has been widely found that sulfate species (i.e., SO_4^{2-}) are a potential stabilizer for maintaining the tetragonal structure of ZrO_2 [56–58]. As shown in Fig. 3a, although its intensity decreases, the diffraction peak of t-ZrO_2 in $Fe_2O_3/ZrO_2@ZrO_2$ persists after sulfurization and regeneration under extreme conditions. A previous study on $Fe_2O_3/ZrO_2@ZrO_2$ confirmed that the t-ZrO_2 phase originates from the ZrO_2 shell [35]. Therefore, the strong binding of SO_4^{2-} to ZrO_2 could contribute to maintain a stable shell in $Fe_2O_3/ZrO_2@ZrO_2$ during H_2S-induced sulfurization and CO_2-enabled regeneration processes. EDX elemental mapping of the sulfurized and regenerated $Fe_2O_3/ZrO_2@ZrO_2$ directly visualizes the difference in the distribution of sulfur (Fig. 5): sulfur species accumulated on Fe are mostly eliminated after regeneration, while residual sulfur persists on Zr. Nonetheless, the majority of accumulated sulfur on $Fe_2O_3/ZrO_2@ZrO_2$ (91 %) can be removed during regeneration (Table S3), which is significantly more effective than the removal of sulfur from sulfurized bare Fe_2O_3 (compare Fig. 5 with Fig. S8). Bare Fe_2O_3 material rapidly transforms into Fe_7S_8 during sulfurization at 750 °C (Fig. S9), which remains unchanged after CO_2 treatment, indicating failure of regeneration. EDX mapping (Fig. S8) and quantitative analysis (Table S3) further confirm that most sulfur ($\sim$ 84 %) accumulated on bare Fe_2O_3 remains present after regeneration.

The oxidation of iron sulfides (i.e., the reactions occurring during regeneration) mainly depends on operating temperature, partial pressure of the oxidant and the particle sizes [21,59]. Under constant reaction temperature and oxidant composition, smaller iron sulfide particles are more easily oxidized, thereby showing better regeneration performance [22,25]. However, the particle size of iron sulfides easily tends to increase at high temperature due to poor resistance against thermal sintering [22,30]. Fig. 6 displays the crystallite sizes of the representative iron-related phases of bare Fe_2O_3 and $Fe_2O_3/ZrO_2@ZrO_2$ in different states. Overall, the formed iron species (FeS_2 or Fe_7S_8) in the sulfurized samples have smaller crystallite sizes than Fe_2O_3 in the fresh samples, due to the occurrence of crystal structure distortion during sulfurization. For bare Fe_2O_3 (Fig. 6a), Fe_7S_8 is the only iron-related phase in the sulfurized sample and its crystallite size significantly increases (up to $\sim$ 30 nm) with prolonged sulfurization time ($1 \rightarrow 5 \rightarrow$

10 min), indicating particle sintering. After regeneration, Fe_7S_8 is not oxidized to iron oxide, but keeps suffering from sintering (compare S1 with S1_CO₂). For $Fe_2O_3/ZrO_2@ZrO_2$ (Fig. 6b), the crystallite sizes of iron-related phases decrease with increasing sulfurization degree ($Fe_3O_4 \rightarrow FeS_2 \rightarrow Fe_7S_8$), corresponding to longer sulfurization time ($1 \rightarrow 5 \rightarrow$ 30 min). After regeneration, the regained iron oxide phase Fe_3O_4 has a crystallite size of $\sim$ 23 nm, which is only slightly larger than the crystallite size of Fe_2O_3 ($\sim$ 21.5 nm) in the fresh sample. Hence, in contrast to bare Fe_2O_3, the $Fe_2O_3/ZrO_2@ZrO_2$ material displays good resistance to sintering of its sulfurized iron particles. The latter is ascribed to the thermal stability of the ZrO_2 shell and support [35], enabling efficient regeneration of the iron sulfides by CO_2. As such, ZrO_2 will endow $Fe_2O_3/ZrO_2@ZrO_2$ with enhanced cyclic stability in the CCLHGD process.

3.3. Sulfurization and regeneration behavior: role of Fe_2O_3 and ZrO_2

Based on the above results, the behavior of $Fe_2O_3/ZrO_2@ZrO_2$ OCM during sulfurization and regeneration in the present experimental conditions is identified and schematically represented in Fig. 7. During sulfurization, H_2S is captured via reduction of Fe_2O_3 to iron sulfides (including FeS_2, FeS and Fe_7S_8). This is a stepwise process with intermediate formation of Fe_3O_4 and Fe, accompanied by the production of SO_2 and H_2O. The generated SO_2 and H_2O can combine on the surface of ZrO_2 to form stable ZrO_2-SO_4^{2-} bonds, which in turn contribute to stabilize the ZrO_2 shell of $Fe_2O_3/ZrO_2@ZrO_2$. Further, SO_2 can react with H_2S, yielding H_2O and elemental sulfur (Claus reaction). In parallel, thermal decomposition of FeS_2 into FeS (or Fe_7S_8) and S_2 occurs, providing another pathway to elemental sulfur. Additionally, replacement of lattice O (at defective sites) in ZrO_2 by S derived from H_2S dissociation occurs, allowing the replaced O to react with the dissociated H to yield H_2O. The presence of S in the lattice of ZrO_2 is believed to improve the mobility of lattice oxygen, thereby enhancing its surface basicity and redox properties, which is beneficial for CO_2 adsorption and activation on the sulfurized $Fe_2O_3/ZrO_2@ZrO_2$ material.

During regeneration by CO_2, dissociation is the initial step and the resulting O oxidizes the iron sulfides to iron oxides, while the sulfur species release in form of SO_2. Moreover, S in the ZrO_2 lattice can be resubstituted by the dissociated O, involving the extraction of sulfur with formation of SO_2 and concomitant refilling of lattice oxygen, leaving only sulfate species at the ZrO_2 surface. Overall, the entire process reaches a sulfur removal efficiency of more than 90 % over the core-shell $Fe_2O_3/ZrO_2@ZrO_2$ material, which in combination with the efficient sintering resistance is the key to success of CCLHGD.
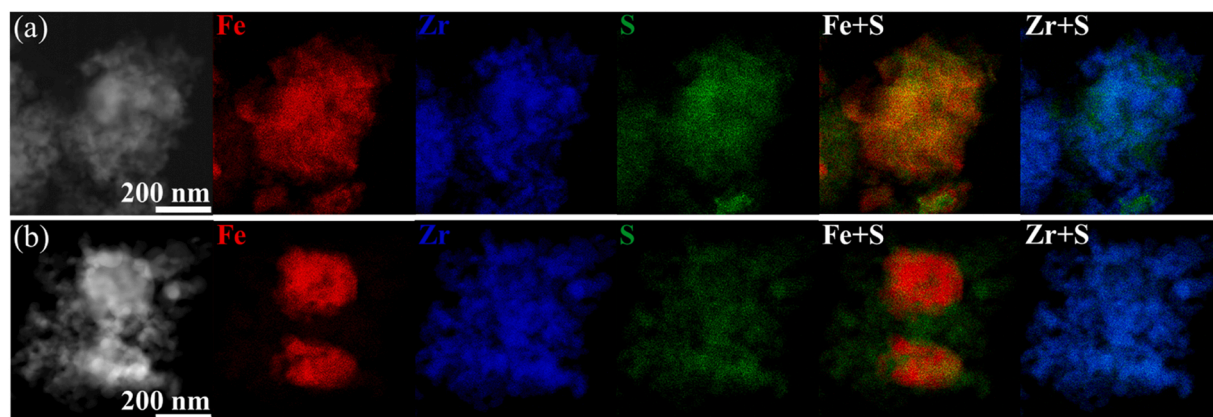

Fig. 5. STEM-EDX mapping of Fe (red), Zr (blue) and S (green) elements and their overlays (Fe+S, Zr+S) for the $Fe_2O_3/ZrO_2@ZrO_2$ material after (a) sulfurization (in pure H_2S at 750 ℃ for 1 min) and (b) regeneration (in pure CO_2 at 700 ℃ for 30 min).
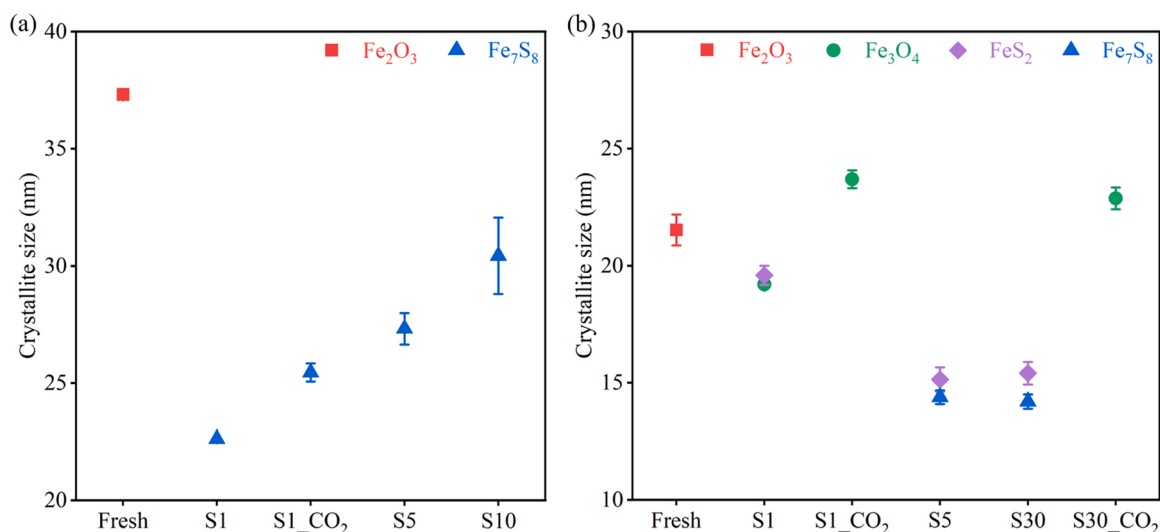
Fig. 6. Crystallite sizes of the representative iron-related phases for (a) bare Fe_2O_3 and (b) $Fe_2O_3/ZrO_2@ZrO_2$ in fresh, sulfurized (by pure H_2S at 750 °C for different durations) and regenerated (by pure CO_2 at 700 °C for 30 min) states. Crystallite size and error bar (i.e., standard deviation) are estimated from Gaussian fitting of the characteristic XRD peaks (as seen in Figs. S9 and 3a). Sample label: for example, S1 represents sulfurization for 1 min; the regenerated samples are marked with _CO_2.
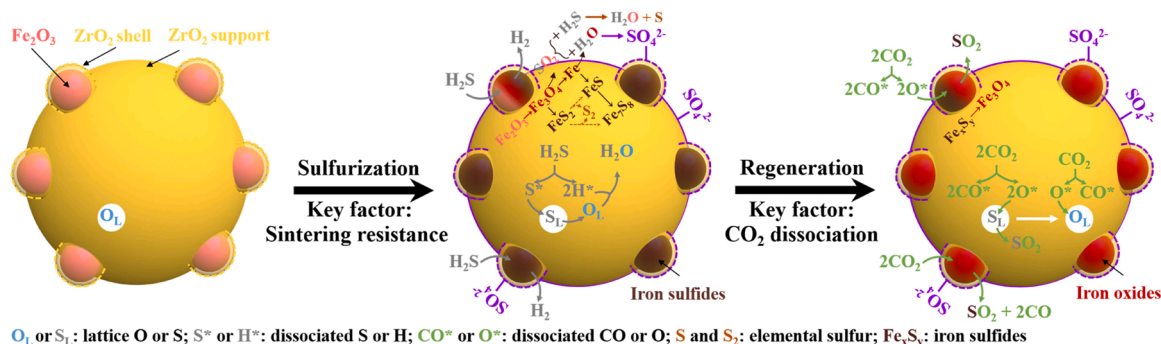

O_L or S_L: lattice O or S; S^* or H^*: dissociated S or H; CO^* or O^*: dissociated CO or O; S and S_2: elemental sulfur; Fe_xS_y: iron sulfides

Fig. 7. Schematic representation of the sulfurization (with H_2S) and regeneration (with CO_2) behavior of the $Fe_2O_3/ZrO_2@ZrO_2$ material in the CCLHGD process.

4. Conclusions

CO_2-assisted Chemical Looping Hot Gas Desulfurization (CCLHGD) is proposed as novel efficient process for high temperature H_2S removal. A core-shell structured $Fe_2O_3/ZrO_2@ZrO_2$ oxygen carrier serves as H_2S sorbent to endow this process with CO_2 affinity. In CCLHGD, the $Fe_2O_3/ZrO_2@ZrO_2$ material experiences alternating sulfurization and regeneration steps: firstly, iron oxides are sulfurized by H_2S to form iron sulfides (sulfur capture); the latter are subsequently regenerated by CO_2 to regain iron oxides, while releasing SO_2 (sulfur removal). Fixed-bed experiments (at 750 °C) and in-situ XAS studies (at 500 °C) with a H_2 and H_2S mixture for sulfurization and diluted CO_2 for regeneration show that an isothermal CCLHGD process can be achieved on $Fe_2O_3/ZrO_2@ZrO_2$.

Ex-situ XRD, XPS and XANES data and STEM characterizations after pure H_2S and pure CO_2 treatment are combined with thermodynamic analysis to emphasize the role of Fe_2O_3 and ZrO_2 during the sulfurization and regeneration of $Fe_2O_3/ZrO_2@ZrO_2$. During sulfurization, Fe_2O_3 transforms step by step into iron sulfides (FeS_2, FeS and Fe_7S_8) with Fe_3O_4 and Fe as transition phases. Subsequently, all iron sulfide phases can be oxidized to iron oxides by oxygen stemming from dissociated CO_2 during regeneration. Furthermore, a reversible substitution of S for O, i. e., consumption (via H_2S during sulfurization) and replenishment (via dissociated CO_2 during regeneration) of lattice oxygen, occurs on ZrO_2, which further enhances the H_2S removal. In addition, compared to bare Fe_2O_3, $Fe_2O_3/ZrO_2@ZrO_2$ shows a good resistance to sintering of

sulfurized iron particles, thanks to the thermally stable ZrO_2 shell and support, thereby ensuring regenerability toward oxidation with CO_2.

CRediT authorship contribution statement

Jiawei Hu: Conceptualization, Methodology, Investigation, Writing - Original Draft; **Hilde Poelman:** Formal analysis, Investigation, Writing - Review & Editing; **Stavros-Alexandros Theofanidis:** Formal analysis, Investigation, Writing - Review & Editing; **Jonas J. Joos:** Investigation, Writing - Review & Editing; **Christophe Detavernier:** Resources, Writing - Review & Editing; **Dirk Poelman:** Resources, Writing - Review & Editing; **Wei Wei:** Supervision, Writing - Review & Editing; **Vladimir V. Galvita:** Supervision, Conceptualization, Methodology, Writing - Review & Editing.

Declaration of Competing Interest

The authors declare that they have no known competing financial interests or personal relationships that could have appeared to influence the work reported in this paper.

Data Availability

Data will be made available on request.

Acknowledgements

Appendix A. Supporting information

Supplementary data associated with this article can be found in the online version at doi:10.1016/j.apcatb.2023.122591.

References

[1] M. Wu, Z. Su, H. Fan, J. Mi, New way of removing hydrogen sulfide at a high temperature: Microwave desulfurization using an iron-based sorbent supported on active coke, Energy Fuels 31 (2017) 4263–4272.

[2] M. Khabazipour, M. Anbia, Removal of hydrogen sulfide from gas streams using porous materials: a review, Ind. Eng. Chem. Res. 58 (2019) 22133–22164.

[3] X. Zhang, Y. Tang, S. Qu, J. Da, Z. Hao, H$_2$S-selective catalytic oxidation: catalysts and processes, ACS Catal. 5 (2015) 1053–1067.

[4] M. Sun, X. Wang, Y. Li, Z. Zhao, J. Qiu, Selective catalytic oxidation of pollutant H$_2$S over Co-decorated hollow N-doped carbon nanofibers for high-performance Li-S batteries, Appl. Catal. B: Environ. 317 (2022), 121763.

[5] A.G. Georgiadis, N.D. Charisiou, M.A. Goula, Removal of hydrogen sulfide from various industrial gases: a review of the most promising adsorbing materials, Catalysts 10 (2020) 521.

[6] S.-A. Theofanidis, J.A.Z. Pieterse, H. Poelman, A. Longo, M.K. Sabbe, M. Virginie, C. Detavernier, G.B. Marin, V.V. Galvita, Effect of Rh in Ni-based catalysts on sulfur impurities during methane reforming, Appl. Catal. B: Environ. 267 (2020), 118691.

[7] Y.H. Lin, Y.C. Chen, H. Chu, The mechanism of coal gas desulfurization by iron oxide sorbents, Chemosphere 121 (2015) 62–67.

[8] T. Li, X. Ren, L. Bao, M. Wang, W. Bao, L. Chang, Effect of lignite as support precursor on deep desulfurization performance of semicoke supported zinc oxide sorbent in hot coal gas, RSC Adv. 10 (2020) 12780–12787.

[9] H. Xia, B. Liu, Q. Li, Z. Huang, A.S.-C. Cheung, High capacity Mn-Fe-Mo/FSM-16 sorbents in hot coal gas desulfurization and mechanism of elemental sulfur formation, Appl. Catal. B: Environ. 200 (2017) 552–565.

[10] S. Cheah, D.L. Carpenter, K.A. Magrini-Bair, Review of mid- to high-temperature sulfur sorbents for desulfurization of biomass- and coal-derived syngas, Energy Fuels 23 (2009) 5291–5307.

[11] D. Liu, Q. Wang, J. Wu, Y. Liu, A review of sorbents for high-temperature hydrogen sulfide removal from hot coal gas, Environ. Chem. Lett. 17 (2018) 259–276.

[12] V. Marcantonio, E. Bocci, J.P. Ouweltjes, L. Del Zotto, D. Monarca, Evaluation of sorbents for high temperature removal of tars, hydrogen sulphide, hydrogen chloride and ammonia from biomass-derived syngas by using Aspen Plus, Int. J. Hydrog. Energy 45 (2020) 6651–6662.

[13] Q. Liu, Z. Zhang, B. Liu, H. Xia, Rare earth oxide doping and synthesis of spinel ZnMn$_2$O$_4$/KIT-1 with double gyroidal mesopores for desulfurization nature of hot coal gas, Appl. Catal. B: Environ. 237 (2018) 855–865.

[14] B.S. Liu, X.N. Wei, Y.P. Zhan, R.Z. Chang, F. Subhan, C.T. Au, Preparation and desulfurization performance of LaMeOx/SBA-15 for hot coal gas, Appl. Catal. B: Environ. 102 (2011) 27–36.

[15] J. Hu, V.V. Galvita, H. Poelman, G.B. Marin, Advanced chemical looping materials for CO$_2$ utilization: a review, Materials 11 (2018) 1187.

[16] L.C. Buelens, H. Poelman, G.B. Marin, V.V. Galvita, 110th anniversary: carbon dioxide and chemical looping: current research trends, Ind. Eng. Chem. Res. 58 (2019) 16235–16257.

[17] L. Zeng, Z. Cheng, J.A. Fan, L.-S. Fan, J. Gong, Metal oxide redox chemistry for chemical looping processes, Nat. Rev. Chem. 2 (2018) 349–364.

[18] X. Zhu, Q. Imtiaz, F. Donat, C.R. Müller, F. Li, Chemical looping beyond combustion – a perspective, Energy Environ. Sci. 13 (2020) 772–804.

[19] T. Kane, J. Guerrero-Caballero, A. Löfberg, H$_2$S chemical looping selective and preferential oxidation to sulfur by bulk V$_2$O$_5$, Appl. Catal. B: Environ. 265 (2020), 118566.

[20] M. Wu, T. Li, H. Li, H. Fan, J. Mi, Desulfurization of hot coal gas over regenerable low-cost Fe$_2$O$_3$/mesoporous Al$_2$O$_3$ prepared by the sol–gel method, Energy Fuels 31 (2017) 13921–13932.

[21] Y.-M. Su, C.-Y. Huang, Y.-P. Chyou, K. Svoboda, Sulfidation/regeneration multi-cyclic testing of Fe$_2$O$_3$/Al$_2$O$_3$, Sorbents High. -Temp. Remov. Hydrog. sulfide, J. Taiwan Inst. Chem. Eng. 74 (2017) 89–95.

[22] Y. Feng, J. Wen, Y. Hu, B. Wu, M. Wu, J. Mi, Evaluation of the cycling performance of a sorbent for H$_2$S removal and simulation of desulfurization-regeneration processes, Chem. Eng. J. 326 (2017) 1255–1265.

[23] N.P. Alderman, V. Peneau, C.J. Viasus, I. Korobkov, B. Vidjayacoumar, K. Albahily, S. Gambarotta, Syn-gas from waste: the reduction of CO$_2$ with H$_2$S, React. Chem. Eng. 4 (2019) 763–771.

[24] C. Cara, E. Rombi, A. Musinu, V. Mameli, A. Ardu, M. Sanna Angotzi, L. Atzori, D. Niznansky, H.L. Xin, C. Cannas, MCM-41 support for ultrasmall γ-Fe$_2$O$_3$ nanoparticles for H$_2$S, Remov., J. Mater. Chem. A 5 (2017) 21688–21698.

[25] H. Tian, J. Wu, W. Zhang, S. Yang, F. Li, Y. Qi, R. Zhou, X. Qi, L. Zhao, X. Wang, High performance of Fe nanoparticles/carbon aerogel sorbents for H$_2$S Removal, Chem. Eng. J. 313 (2017) 1051–1060.

[26] V.V. Galvita, H. Poelman, E. Fornero, M. Saeys, G.B. Marin, Development and performance of iron based oxygen carriers for chemical looping, in: M.Vd Voorde, B. Sels (Eds.), Nanotechnology in Catalysis, 2017, pp. 421–448.

[27] L.C. Buelens, A. Van Alboom, H. Poelman, C. Detavernier, G.B. Marin, V.V. Galvita, Fe$_2$O$_3$–MgAl$_2$O$_4$ for CO production from CO$_2$: Mössbauer spectroscopy and in situ x-ray diffraction, ACS Sustain. Chem. Eng. 7 (2019) 9553–9565.

[28] F. Donat, C.R. Müller, CO$_2$-free conversion of CH$_4$ to syngas using chemical looping, Appl. Catal. B: Environ. 278 (2020), 119328.

[29] B. Jin, H. Poelman, C. Detavernier, Z. Liang, G.B. Marin, V.V. Galvita, Microstructured ZrO$_2$ coating of iron oxide for enhanced CO$_2$ conversion, Appl. Catal. B: Environ. 292 (2021), 120194.

[30] J. Hu, H. Poelman, G.B. Marin, C. Detavernier, S. Kawi, V.V. Galvita, FeO controls the sintering of iron-based oxygen carriers in chemical looping CO$_2$ conversion, J. CO$_2$ Util. 40 (2020), 101216.

[31] E.I. Kauppi, E.H. Rönkkönen, S.M.K. Airaksinen, S.B. Rasmussen, M.A. Bañares, A.O.I. Krause, Influence of H$_2$S on ZrO$_2$-based gasification gas clean-up catalysts: MeOH temperature-programmed reaction study, Appl. Catal. B: Environ. 111–112 (2012) 605–613.

[32] K.V. Jangam, A.S. Joshi, Y.-Y. Chen, S. Mahalingam, A.A. Sunny, L.-S. Fan, Synergistic decomposition of H$_2$S into H$_2$ by Ni$_3$S$_2$ over ZrO$_2$ support via a sulfur looping scheme with CO$_2$ enabled carrier regeneration, Chem. Eng. J. 426 (2021), 131815.

[33] E.I. Kauppi, J.M. Kanervo, J. Lehtonen, L. Lefferts, Interaction of H$_2$S with ZrO$_2$ and its influence on reactivity of surface oxygen, Appl. Catal. B: Environ. 164 (2015) 360–370.

[34] E.I. Kauppi, K. Honkala, A.O.I. Krause, J.M. Kanervo, L. Lefferts, ZrO$_2$ acting as a redox catalyst, Top. Catal. 59 (2016) 823–832.

[35] J. Hu, V.V. Galvita, H. Poelman, C. Detavernier, G.B. Marin, A core-shell structured Fe$_2$O$_3$/ZrO$_2$@ZrO$_2$ nanomaterial with enhanced redox activity and stability for CO$_2$ conversion, J. CO$_2$ Util. 17 (2017) 20–31.

[36] P. Scherrer, Nachrichten von der Gesellschaft, der Wissenschaften zu Göttingen, Weidmannsche Buch 26 (1918) 98–100.

[37] C. Cui, Y. Liu, S. Mehdi, H. Wen, B. Zhou, J. Li, B. Li, Enhancing effect of Fe-doping on the activity of nano Ni catalyst towards hydrogen evolution from NH$_3$BH$_3$, Appl. Catal. B: Environ. 265 (2020), 118612.

[38] M.A. Fahim, T.A. Alsahhaf, A. Elkilani, Chapter 15 - acid gas processing and mercaptans removal, in: M.A. Fahim, T.A. Alsahhaf, A. Elkilani (Eds.), Fundamentals of Petroleum Refining, Elsevier, Amsterdam, 2010, pp. 377–402.

[39] Y. Zhang, Q. Li, X. Liu, B. Xu, Y. Yang, T. Jiang, A thermodynamic analysis on the roasting of pyrite, Minerals 9 (2019) 220.

[40] W. Lv, D. Yu, J. Wu, L. Zhang, M. Xu, The chemical role of CO$_2$ in pyrite thermal decomposition, Proc. Combust. Inst. 35 (2015) 3637–3644.

[41] F. Huang, L.-Q. Zhang, B.-J. Yi, Z.-J. Xia, C.-G. Zheng, Transformation pathway of excluded mineral pyrite decomposition in CO$_2$ atmosphere, Fuel Process. Technol. 138 (2015) 814–824.

[42] Y. Yang, J. Liu, Z. Wang, F. Liu, J. Ding, CO$_2$-mediated sulfur evolution chemistry of pyrite oxidation during oxy-fuel combustion, Combust. Flame 218 (2020) 75–83.

[43] X. Ren, L. Chang, F. Li, K. Xie, Study of intrinsic sulfidation behavior of Fe$_2$O$_3$ for high temperature H$_2$S removal, Fuel 89 (2010) 883–887.

[44] H. Lv, H. Zhao, T. Cao, L. Qian, Y. Wang, G. Zhao, Efficient degradation of high concentration azo-dye wastewater by heterogeneous Fenton, Process iron-Based Met. -Org. Framew., J. Mol. Catal. A: Chem. 400 (2015) 81–89.

[45] H. van der Heide, R. Hemmel, C.F. van Bruggen, C. Haas, X-ray photoelectron spectra of 3d transition metal pyrites, J. Solid State Chem. 33 (1980) 17–25.

[46] H. Kohzadi, M. Soleiman-Beigi, XPS and structural studies of Fe$_3$O$_4$-PTMS-NAS@ Cu as a novel magnetic natural asphalt base network and recoverable nanocatalyst for the synthesis of biaryl compounds, Sci. Rep. 11 (2021) 24508.

[47] M. Mullet, S. Boursiquot, M. Abdelmoula, J.-M. Génin, J.-J. Ehrhardt, Surface chemistry and structural properties of mackinawite prepared by reaction of sulfide ions with metallic iron, Geochim. Cosmochim. Acta 66 (2002) 829–836.

[48] A. Matamoros-Veloza, O. Cespedes, B.R.G. Johnson, T.M. Stawski, U. Terranova, N.H. de Leeuw, L.G. Benning, A highly reactive precursor in the iron sulfide system, Nat. Commun. 9 (2018) 3125.

[49] N.R. Urban, K. Ernst, S. Bernasconi, Addition of sulfur to organic matter during early diagenesis of lake sediments, Geochim. Cosmochim. Acta 63 (1999) 837–853.

[50] J. Baltrusaitis, D.M. Cwiertny, V.H. Grassian, Adsorption of sulfur dioxide on hematite and goethite particle surfaces, Phys. Chem. Chem. Phys. 9 (2007) 5542–5554.

[51] X. Zou, X. Wu, Y. Liu, D. Liu, W. Li, L. Gu, H. Liu, P. Wang, L. Sun, Y. Zhang, In situ generation of bifunctional, efficient Fe-based catalysts from mackinawite iron sulfide for water splitting, Chem 4 (2018) 1139–1152.

[52] T.J. Toops, M. Crocker, New sulfur adsorbents derived from layered double hydroxides, Appl. Catal. B: Environ. 82 (2008) 199–207.

[53] M. Ziolek, J. Kujawa, O. Saur, J.C. Lavalley, Influence of hydrogen sulfide adsorption on the catalytic properties of metal oxides, J. Mol. Catal. A: Chem. 97 (1995) 49–55.

[54] J.R. Anderson, H. Kleinke, H.F. Franzen, $ZrO_{2-x}S_x$: Stabilization of cubic ZrO_2 by a partial exchange of oxygen by sulfur, J. Alloy. Compd. 259 (1997) L14–L18.

[55] L. Suthar, F. Bhadala, P. Kumari, S.K. Mishra, M. Roy, Effect of Mn substitution on crystal structure and electrical behaviour of $YFeO_3$ ceramic, Ceram. Int. 47 (2021) 19007–19018.

[56] A.I. Ahmed, S.A. El-Hakam, S.E. Samra, A.A. El-Khouly, A.S. Khder, Structural characterization of sulfated zirconia and their catalytic activity in dehydration of ethanol, Colloids Surf. A 317 (2008) 62–70.

[57] C.D. Miranda M, A.E. Ramírez S, S.G. Jurado, C.R. Vera, Superficial effects and catalytic activity of ZrO_2–SO_4^{2-} as a function of the crystal structure, J. Mol. Catal. A: Chem. 398 (2015) 325–335.

[58] E.M. Kock, M. Kogler, T. Gotsch, L. Schlicker, M.F. Bekheet, A. Doran, A. Gurlo, B. Klotzer, B. Petermuller, D. Schildhammer, N. Yigit, S. Penner, Surface chemistry of pure tetragonal ZrO_2 and gas-phase dependence of the tetragonal-to-monoclinic ZrO_2 transformation, Dalton Trans. 46 (2017) 4554–4570.

[59] M.D. Stephenson, M. Rostam-Abadi, L.A. Johnson, C.W. Kruse, A review of gas phase desulfurization of char, Coal Sci. Technol. 9 (1985) 353–372.